Hindawi
Structural Control and Health Monitoring
Volume 2023, Article ID 6349167, 18 pages
https://doi.org/10.1155/2023/6349167

Research Article

Unsupervised Domain Adaptation Damage Identification Approach of High Arch Dams after Earthquakes

Cao Xiangyu,[1,2] **Chen Liang**,[1] **Chen Jianyun**,[2,3] **Li Jing**,[2,3] **Lu Wenyan**,[1] **Liu Haixiang**,[1] **Pengfei Liu**,[2,3] **Ke Minyong**,[1] **and Tang Yunqing**[1]

[1]*Nanjing Hydraulic Research Institute, Nanjing 210029, China*
[2]*State Key Laboratory of Coastal and Offshore Engineering, Dalian University of Technology, Dalian 116024, China*
[3]*School of Hydraulic Engineering, Faculty of Infrastructure Engineering, Dalian University of Technology, Dalian 116024, China*

Correspondence should be addressed to Chen Jianyun; chenjydg@dlut.edu.cn and Tang Yunqing; yqtang@nhri.cn

Received 3 January 2023; Revised 30 May 2023; Accepted 3 June 2023; Published 24 June 2023

Academic Editor: José Rodellar

In actual concrete arch dam engineering scenarios, the dynamic data obtained by the health monitoring system of an arch dam are incomplete. The data acquired typically depend on the state of the dam structure, that is, whether it is intact or incomplete. Besides, the future environmental loads of the structure are unpredictable. Thus, environmental noise is also uncertain. In practical engineering, the use of a damage identification model constructed based on incomplete information is problematic in scenarios with variable loads. Consequently, detecting the water level in actual arch dam projects after an earthquake and determining the impact of environmental uncertainty are necessary. Accordingly, this paper proposes a denoising contractive sparse deep autoencoder (DCS-DAE) model based on domain adaptation. The core idea of the proposed method is to constrain the data probability distribution of feature spaces in the source and target domains using maximum mean discrepancy. This fusion enables the DCS-DAE model to be capable of feature extraction. Moreover, it resolves the problem in which the objective function cannot be applied to other similar scenarios because of the lack of consistency constraints of feature spaces in the source and target domains. Four working conditions are designed to reproduce the uncertainty of structural modeling and the variability of water levels. The conditions are based on the postseismic water level detection requisites of dams in practical engineering. The results show that the proposed anomaly detection model enhances the generalization performance of the DCS-DAE in terms of feature design. Hence, the constructed model can "infer other things from one fact." The results of this study are meaningful for the real-time cross-domain monitoring of structures under variable load conditions, providing a driving force to apply similar methods to practical arch dam projects.

1. Introduction

Hydraulic structures are among the primary infrastructure affecting national economy. The destruction or collapse of these structures due to events, such as strong earthquakes, can result in mass death, injuries, and extremely severe property losses. Accordingly, the formulation of an accurate, efficient, and intelligent damage warning and identification model for concrete arch dams is necessary to ensure infrastructure safety.

Structural damage identification within the field of structural health monitoring (SHM) has been garnering increasing attention. Vision-based damage identification methods, primarily using image processing techniques (IPTs), have been proposed to redeem the complexities [1–5]. However, hydraulic structures are bulky and a considerable portion of the area is located underwater, making it difficult for vision-based methods to comprehensively detect the structure in a short period of time. The data-driven damage identification method can effectively solve this problem. The data-driven damage identification method focuses on the exploration of monitoring data through statistical pattern recognition [6–9] (i.e., the search for correlations, not causality). Fundamentally, the method

identifies different state patterns of the structure according to the probability distribution and evolution law of monitoring data [10–13]. Presently, the exploration of damage identification based on such methods is mainly implemented using small-scale monitoring data. However, performance considering large-scale monitoring data requires further exploration [14]. In terms of statistical process control, damage identification methods can be classified into techniques based on univariate control charts [15] and those that refer to multivariate statistical analysis [16, 17]. Under the action of variable coupling environmental loads, the monitoring signals of different parts of the arch dam typically have cross-correlations. Hence, a method based on multivariate statistical analysis is more suitable for actual engineering scenarios. With the rapid development of sensing technology and data acquisition systems in recent years, the theory of damage identification based on big data has flourished. Moreover, various damage identification methods based on deep learning have emerged [18–23]. The foregoing type of damage identification typically involves two steps: feature extraction and pattern matching [24]. Damage identification methods based on supervised learning have been proven to have satisfactory damage identification ability [25, 26]. However, such methods cannot derive the monitoring information of structures under various damage modes [27]. Therefore, research in this field has gradually shifted from diagnoses based on supervised learning to those built on semisupervised and unsupervised learning. Sarmadi and Yuen [28] proposed an unsupervised singular value diagnosis method based on the Foley–Sammon transform of kernel null space that can reduce misdiagnosis in an environment with varying load conditions. Soleimani Babakamali et al. [29] proposed an unsupervised damage identification method that is robust to different sensor placement schemes. The method uses previous data obtained by the structural health monitoring system for feature extraction; hence, the training data are deemed as a type of "prior information." Cha and Wang [30] proposed an unsupervised novelty detection-based density peak-based fast clustering algorithm and verified the advantages of unsupervised learning in the field of damage identification through a laboratory-scale steel structure. Cao et al. [31] proposed a feature extraction method based on unsupervised deep learning and a fast postearthquake damage identification model. This model solves the problems of low measurement accuracy and poor recognition robustness of manually designed damage sensitive features in actual arch dam engineering. However, for the damage identification of arch dams, the "prior information" provided by monitoring data is insufficient.

From a statistical perspective, the measurement threshold for feature classification is determined by analyzing the differences in measurements (such as probability distribution) among multiple sets of data samples. However, due to the limitations of the monitoring system for arch dam, the effectiveness of selecting the measurement threshold may vary in different scenarios. In terms of engineering applications, these methods heavily rely on two requirements: highly accurate numerical models and diverse training scenarios. Regarding the first requirement, it is worth noting that an unsupervised learning model only needs to collect the vibration signal from the intact structure during normal operation. This approach avoids the challenges of gathering sufficient training data from various damage scenarios. However, this method is constrained by the lack of damage information in the training data, which makes it difficult to accurately identify the extent of damage. As for the second requirement, when a large hydraulic structure is affected by an earthquake, the emergency department lowers the water level to mitigate the risk of secondary disasters, such as aftershocks and dam swells. However, this change in water level renders the damage identification model, based on the normal water level of the intact structure, ineffective. In theory, the unsupervised damage detection model constructed using vibration data from the intact structure can only handle a single test scenario. Nevertheless, in practice, there are countless potential test scenarios. Therefore, the unsupervised damage detection model based on the response signal of an intact structure needs to adapt to emerging scenarios.

This study combines knowledge-driven and data-driven methods to obtain features that only reflect the structure. In terms of feature design, the combination is unaffected by the environment. Inspired by transfer learning, the idea of domain adaptation is introduced into the field of structural health monitoring. Accordingly, a common feature extraction model, the denoising contractive sparse deep autoencoder (DCS-DAE) based on domain adaptation, is proposed.

First, the concept of maximum mean discrepancy (MMD) for constraining the data probability distribution of feature spaces in the source and target domains is fused with the DCS-DAE model under the same framework. The fusion enables the newly constructed model to exhibit the feature extraction capability of the DCS-DAE model. Moreover, it resolves the problem in which the objective function cannot be applied to other similar scenarios because of the lack of consistency constraints of feature spaces between the source and target domains. Then, according to the actual operation of the arch dam, four acquisition models of the target domain data are designed with model material error and water level interference considered as uncertain factors. Subsequently, the test results are compared and discussed. The proposed approach enhances the generalization performance of the unsupervised anomaly detection model in terms of feature design. The damage identification requisites are also extended such that the constructed detection model has the ability to "infer from others." The configuration of the computer is 16.0 GB RAM and Intel Core i9 CPU@ 3.60 GHz.

2. Several Important Considerations

2.1. Contradiction in Data Volume Gap among Different Scenarios. The increase in the number of newly devised machine learning-based feature extraction methods relies on a considerable amount of available training data. For general supervised learning, sufficient labeled data are required

[32–34]; for general unsupervised learning, sufficient data from the same scene are necessary [35–37]. However, in actual large-scale water conservation projects, high-quality data are missing. In some data centers, only training data on a certain scenario (such as the state of structural loss) are available, whereas those on other scenarios (e.g., the state of structural damage) are insufficient. The damage identification method based on unsupervised learning presents an innovative solution to this problem of training data insufficiency. However, the output signal characteristics of the structure depend not only on system properties (i.e., state of the structure) but also on system input (i.e., state of the load).

Specifically, for arch dams under normal reservoir operations, the water impounded by the dam is typically stored at a normal water level to profit from dam operation as designed. Moreover, at this water level, the amount of dam vibration data is abundant; the information can be utilized to adjust runoff and increase the output of the hydropower station. When the water height is between the constant and dead water levels, the amount of vibration data is large. Under normal reservoir operations, the lowest water level allowed for the reservoir is the dead water level. In particular scenarios, such as during dry years or periods of combat readiness, the lowest water level allowed is the limit dead water level. These two types of scenarios are special; hence, the data associated with these two water levels are scarce. Overall, leveraging the vibration data of the structure when the water height is close to the normal level yields greater advantages compared to utilizing data from a different water level.

2.2. Contradiction between Big Data and Weak Computing. The level of water impounded by the reservoir is infinite, and the vibration data of the structure corresponding to other water levels are extremely scarce. Variations in the amount of data under different scenarios may be ignored, and the vibration data of the structure at different water levels may be assumed sufficient. Nevertheless, constructing multiple anomaly detection models considering variable water levels after an earthquake is unrealistic. Big data require high-performance computing equipment for storage and calculation. However, not every water conservancy project is worth the cost of purchasing expensive computing equipment. Consequently, a contradiction between big data and weak computing exists. In other words, when high-performance computers are not available, the use of massive data to train a model is a hardware problem. An effective approach to solve this problem is the implementation of transfer learning.

2.3. Contradiction between Generalized Model and Requisites of Specific Scenarios. With rapid developments in sensing, storage, and signal processing technologies, the long-term tracking and processing of the dam body response are no longer a problem. For example, strong-motion seismometers are widely used for monitoring large dams. In the field of monitoring the health of large hydraulic structures, damage identification based on machine learning is a prerequisite because considerable amounts of dam response data are available. First, rapid model building must be possible to satisfy emergency requirements after an earthquake. Second, the model must have strong generalization capability, that is, although the built models may be few, they can be applied to as many scenarios as possible. For traditional machine learning methods, the typical assumption is that newly acquired data follow the same distribution as the original data. However, in structural health monitoring, this assumption is difficult to sustain. In view of this, a well-fitted model is adapted and transformed according to a small amount of data obtained from different scenarios. The model strives to be "unchangeable and adapts to all changes," such that it can be effective for anomaly detection tasks in specific scenarios.

3. Methodology

3.1. Domain Adaptation Techniques. Domain $\mathscr{D}$ is the subject of transfer learning and consists of two parts: feature space, $\mathscr{X}$ (data), and marginal probability distribution ($P(X)$). Here, $X = \{x_1, x_2, \ldots, x_n\} \in \mathscr{X}$ represents field data; it is a type of matrix, where x_i represents the i^{th} sample or feature [38]. The marginal probability distribution, $P(X)$, is a logical concept, and different fields can be considered to have varied probability distributions. Because transfer learning is involved, two fundamental domains are considered: source domain ($\mathscr{D}_s$) and target domain ($\mathscr{D}_t$). Transfer is achieved when knowledge propagates from $\mathscr{D}_s$ to $\mathscr{D}_t$.

Correspondingly, task $\mathscr{T}$ is the learning target, which also consists of two parts: label space $\mathscr{Y}$ and learning function $f(\bullet)$. The label space of the source and target domains can be expressed as $\mathscr{Y}_s$ and $\mathscr{Y}_t$, respectively, and the class labels of actual samples in the source and target domains can be expressed as y_s and y_t, respectively. In fact, in most real production activities, the data labels of the target domain are not available, and unsupervised methods are easily extended to supervised methods. Consequently, a key research area in current transfer learning is unsupervised transfer learning. Unless otherwise specified, the following discussion concerns unsupervised transfer learning. Specifically, $\mathscr{D}_s = \{x_{s_i}, y_{s_i}\}_{i=1}^{n_s}$ represents the labeled data of the source domain, where $x_{s_i} \in \mathscr{X}_s$ and $y_{s_i} \in \mathscr{Y}_s$. Similarly, $\mathscr{D}_t = \{x_{t_i}\}_{i=1}^{n_t}$ represents the unlabeled target domain data, where $x_{t_i} \in \mathscr{X}_t$.

Consider a given labeled source domain, $\mathscr{D}_s = \{x_{s_i}, y_{s_i}\}_{i=1}^{n_s}$ (n_s is the number of samples in the source domain), and an unlabeled target domain, $\mathscr{D}_t = \{x_{t_i}\}_{i=1}^{n_t}$ (n_t is the number of samples in the target domain). The marginal probability distributions for the two domains differ, that is, $P_s(x_s) \neq P_t(x_t)$. The goal of transfer learning is to learn a classifier, $f: x_t \longrightarrow y_t$, by virtue of $\mathscr{D}_s$ to predict the label ($y_t \in \mathscr{Y}_t$) [39]. Consider a given labeled source domain, $\mathscr{D}_s = \{x_{s_i}, y_{s_i}\}_{i=1}^{n_s}$, and an unlabeled target domain, $\mathscr{D}_t = \{x_{t_i}\}_{i=1}^{n_t}$. If the feature spaces of the two fields are the same ($\mathscr{X}_s = \mathscr{X}_t$), then the label space and conditional probability distribution are also the same, i.e., $\mathscr{Y}_s = \mathscr{Y}_t$ and $Q_s(x_s \mid y_s) = Q_t(x_t \mid y_t)$, respectively. However, the two

domains have different marginal probability distributions ($P_s(x_s) \neq P_t(x_t)$). The purpose of the domain adaptation method is to learn a classifier, $f: x_t \longrightarrow y_t$, using the source domain, $\mathscr{D}_s$, to predict the label, $y_t \in \mathscr{Y}_t$, of the target domain, $\mathscr{D}_t$. Similar to the domain adaptation method, the core of the deep domain adaptation method is to learn a deep neural network, $f: x_t \longrightarrow y_t$, to predict the label, $y_t \in \mathscr{Y}_t$, of the target domain, $\mathscr{D}_t$, using the source domain, $\mathscr{D}_s$.

3.2. Cross-Domain Feature Adaptation. In this study, the core idea of cross-domain feature adaptation is to transform knowledge from the source domain (i.e., sufficient arch dam vibration data at normal water levels) to the target domain (i.e., insufficient arch dam vibration data at other water levels) for knowledge acquisition. The structural information obtained from a structure at a certain water level is considered beneficial for acquiring knowledge of the structural state at another water level. In other words, the mechanical nature of damage to the structure at different water levels is similar.

Consistency constraints of feature spaces between the source and target domains in the objective function are lacking. Thus, when the data distributions of the source and target domains considerably differ, the feature extractor based on the DCS-DAE model is probably based on data with considerable distribution differences. Consequently, more data features can be derived, increasing the variation in the original data distribution. As shown in Figure 1(a), reconstruction becomes more problematic [40]. By contrast, cross-domain feature adaptation can use metrics to constrain the data probability distribution of feature spaces in the source and target domains for extracting common features, as shown in Figure 1(b).

3.3. MMD in Reproducing Kernel Hilbert Space. Suppose $\mathscr{F}$ is a set of functions ($f: \mathscr{X} \longrightarrow R$), p and q conform to probability distributions, and two sets of data, $X = (x_1, x_2, \ldots, x_m)$ and $Y = (y_1, y_2, \ldots, y_n)$, are independent and identically distributed samples collected from p and q, respectively. The MMD and its empirical estimation are defined as follows [41–43]:

$$\mathrm{MMD}[\mathscr{F}, p, q] \coloneqq \sup_{f \in \mathscr{F}} \left(\mathrm{E}_{x \sim p}[f(x)] - \mathrm{E}_{y \sim q}[f(y)] \right), \tag{1}$$

$$\mathrm{MMD}[\mathscr{F}, X, Y] \coloneqq \sup_{f \in \mathscr{F}} \left(\frac{1}{m} \sum_{i=1}^{m} f(x_i) - \frac{1}{n} \sum_{i=1}^{n} f(y_i) \right), \tag{2}$$

where $\sup_{f \in \mathscr{F}}(\cdot)$ denotes supremum. To measure the difference between two sets of data effectively, the following two requirements are required for the function space, $\mathscr{F}$. (1) When p and q have the same distribution, MMD $[\mathscr{F}, p, q]$ is equal to zero. (2) As the size of the observation set increases, MMD $[\mathscr{F}, p, q]$ can quickly converge to its expectation. Accordingly, Gretton et al. [44] elaborated on various function spaces and pointed out that when using a unit ball in reproducing kernel Hilbert space (RKHS) as the function space, effective trade-off can be achieved for the two foregoing requirements.

Using the RKHS, equation (1) can be expressed as follows:

$$\begin{aligned} \mathrm{MMD}[p, q] &\coloneqq \sup_{f \in \mathscr{F}} \left(\mathrm{E}_{x \sim p}[f(x)] - \mathrm{E}_{y \sim q}[f(y)] \right) \\ &= \sup_{\|f\|_{\mathscr{H}} \leq 1} \left(\mathrm{E}_{x \sim p}[\langle f, \phi(x) \rangle_{\mathscr{H}}] - \mathrm{E}_{y \sim q}[\langle f, \phi(y) \rangle_{\mathscr{H}}] \right) \\ &= \sup_{\|f\|_{\mathscr{H}} \leq 1} \left(\langle f, \mathrm{E}_{x \sim p}[\phi(x)] \rangle_{\mathscr{H}} - \langle f, \mathrm{E}_{y \sim q}[\phi(y)] \rangle_{\mathscr{H}} \right) \\ &= \sup_{\|f\|_{\mathscr{H}} \leq 1} \left(\langle f, \mu_p - \mu_q \rangle_{\mathscr{H}} \right) = \left\| \mu_p - \mu_q \right\|_{\mathscr{H}}. \end{aligned} \tag{3}$$

Thus far, the calculation method for the MMD in the RKHS has been derived. However, the problem is that the mapping, $\phi(x)$, is not determinable. As presented in the previous section, the kernel function can be imagined as obtained by multiplying the mapping. The mapping can be determined by obtaining the square of equation (1) and applying the kernel technique to derive the following:

$$\begin{aligned} \mathrm{MMD}^2[p, q] &= \langle \mu_p - \mu_q, \mu_p - \mu_q \rangle_{\mathscr{H}} \\ &= \langle \mu_p, \mu_p \rangle_{\mathscr{H}} + \langle \mu_q, \mu_q \rangle - 2\langle \mu_p, \mu_q \rangle_{\mathscr{H}} \\ &= \mathrm{E}_p[\langle \phi(x), \phi(x') \rangle_{\mathscr{H}}] + \mathrm{E}_q[\langle \phi(y), \phi(y') \rangle_{\mathscr{H}}] - \mathrm{E}_{p,q}[\langle \phi(x), \phi(y) \rangle_{\mathscr{H}}] \\ &= \mathrm{E}_p[K(x, x')] + \mathrm{E}_q[K(y, y')] - 2\mathrm{E}_{p,q}[K(x, y)]. \end{aligned} \tag{4}$$

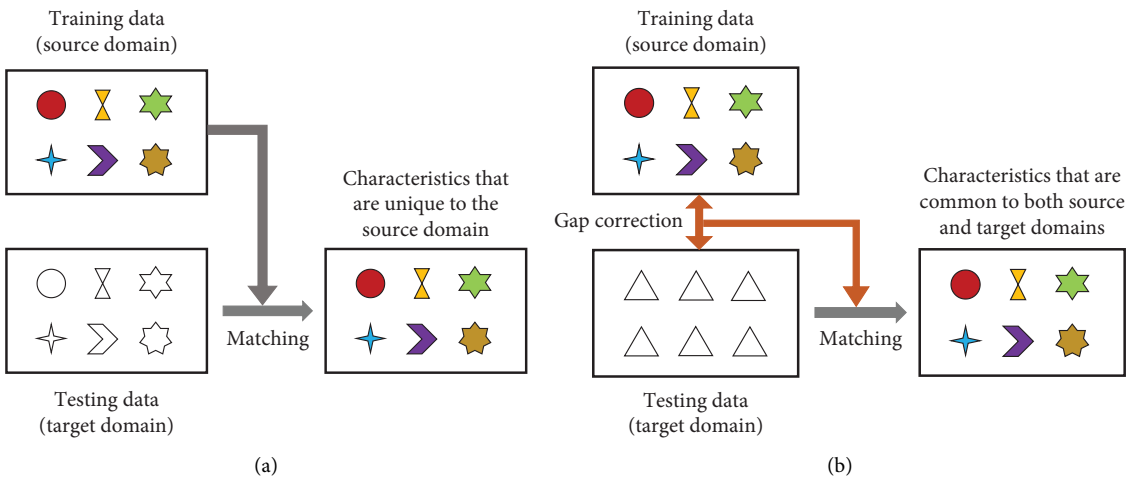

Figure 1: Comparison of methods for solving cross-domain identification problems. (a) Traditional process for resolving cross-domain identification problems. (b) Solving process of cross-domain identification problems based on transfer learning.

If two sets of data, $X = (x_1, x_2, \ldots, x_m)$ and $Y = (y_1, y_2, \ldots, y_n)$, are independent and identically distributed samples collected from p and q, respectively, then the empirical estimate of equation (4) can be deduced as

$$\mathrm{MMD}^2[X,Y] \coloneqq \frac{1}{m^2}\sum_{i,j=1}^{m} K\left(x_i, x_j\right) + \frac{1}{n^2}\sum_{i,j=1}^{n} K\left(y_i, y_j\right) - \frac{2}{mn}\sum_{i,j=1}^{m,n} K\left(x_i, y_j\right). \tag{5}$$

3.4. Unsupervised Domain Adaptation Techniques Based on DCS-DAE

3.4.1. Framework of Model and Objective Function. The DCS-DAE is an improved feature extractor based on unsupervised learning [25, 31, 45], which can realize anomaly diagnosis using reconstruction error and boxplot [46, 47] as well as achieve anomaly localization through the weighted K-nearest neighbor algorithm [48]. To improve the abnormal recognition ability of the DCS-DAE model in different structural scenarios, a domain-adaptive DCS-DAE model is proposed. The overall framework of the model is illustrated in Figure 2, where solid lines represent the training process of the unsupervised domain adaptation technique based on DCS-DAE, while dashed lines depict the testing process of vibration response signals under unknown structural conditions. The specific implementation process is shown in Figure 3.

The objective function of the model consists of two parts: the reconstruction error loss of DCS-DAE ($J_{\mathrm{DCS-DAE}}$) and MMD-based probability of the source and target domains with respect to the consistency constraints (J_{MMD}) of feature space distribution. Accordingly, the optimization objective function of this model can be expressed as follows:

$$J = J_{\mathrm{DCS-DAE}} + \lambda J_{\mathrm{MMD}}, \tag{6}$$

where λ is used to weigh the contributions of $J_{\mathrm{DCS-DAE}}$ and J_{MMD} to the objective function.

3.4.2. Training Process and Hyperparameter Settings. The cost function of the model is composed of $J_{\mathrm{DCS-DAE}}$ and J_{MMD}. First, the calculation and optimization of $J_{\mathrm{DCS-DAE}}$ are discussed in this section. The cost functions of the denoising, contractive, and sparse autoencoders are as follows:

$$\begin{aligned} J_{DAE} &= \frac{1}{2N}\sum_{i=1}^{N}\left\|\overline{x}^{(i)} - x^{(i)}\right\|_2^2, \\ J_{CAE} &= J_{\mathrm{AE}} + \psi J_f = \frac{1}{2N}\sum_{i=1}^{N}\left\|x^{(i)} - \overline{x}^{(i)}\right\|_2^2 + \frac{\psi}{2N}\sum_{i=1}^{N}\left\|J_f\left(x^{(i)}\right)\right\|_F^2, \\ J_{SAE} &= J_{\mathrm{AE}} + \frac{\lambda}{2}J_r + \beta J_s \\ &= \frac{1}{2N}\sum_{i=1}^{N}\left\|\overline{x}^{(i)} - x^{(i)}\right\|_2^2 + \frac{\lambda}{2}\left(\left\|W_D\right\|_F^2 + \left\|W_E\right\|_F^2\right) + \beta\left(\sum_{j=1}^{m}\rho\log\left(\frac{\rho}{\rho_j'}\right) + (1-\rho)\log\left(\frac{1-\rho}{1-\rho_j'}\right)\right), \end{aligned} \tag{7}$$

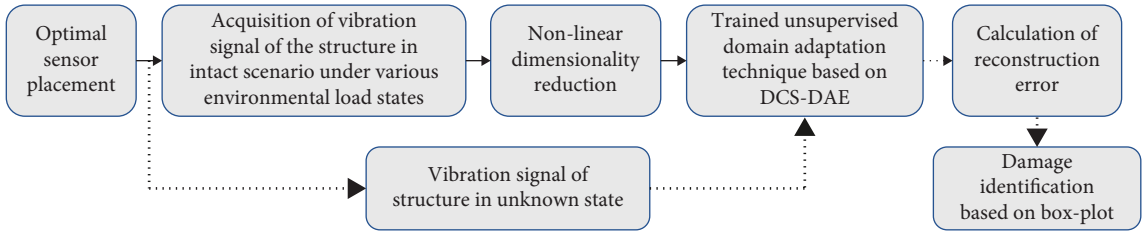

FIGURE 2: Schematic diagram of the proposed unsupervised domain adaptation technique based on DCS-DAE.

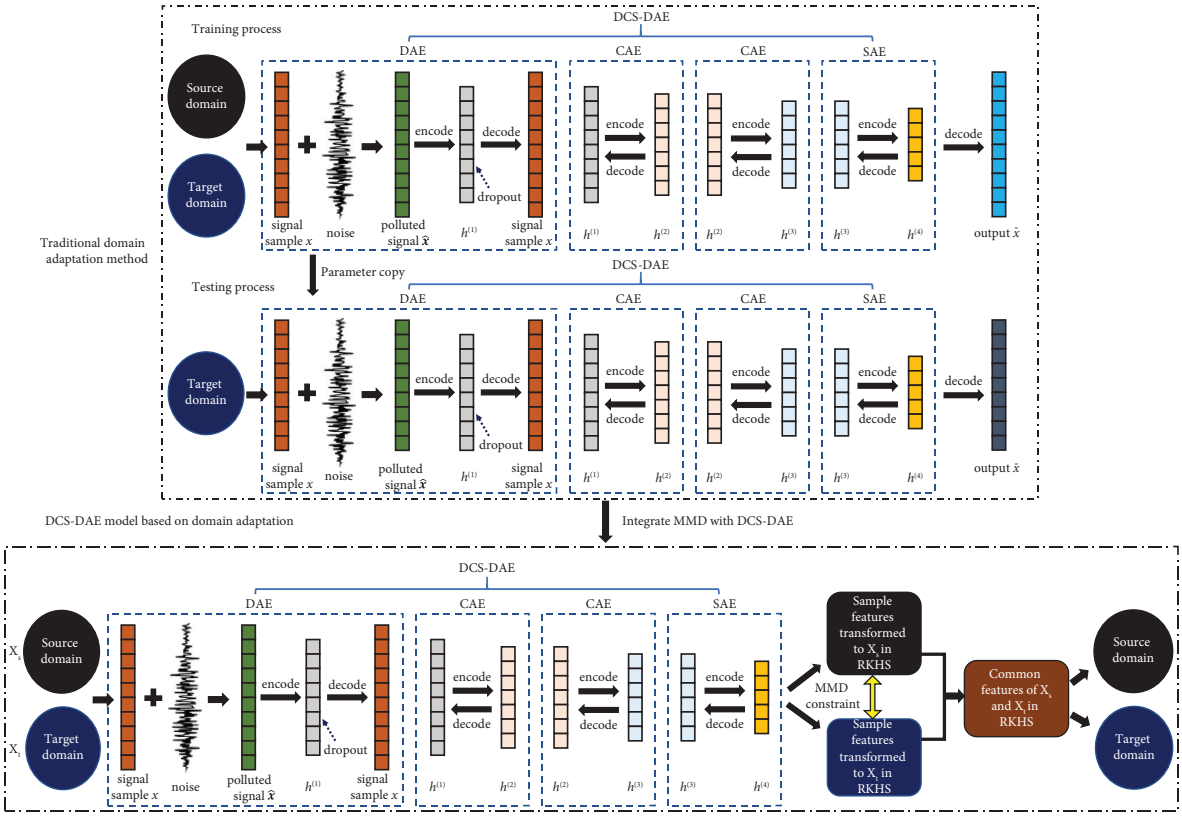

FIGURE 3: Architecture and improved process of domain adaptation technique based on DCS-DAE.

where i and N represent the sample number and total number of samples, respectively; $\|\cdot\|_2$ indicates the L2 norm; $J_f(x^{(i)})$ represents the Jacobian penalty; ψ is the shrinkage coefficient; λ is the norm weight; β is the sparse rate; and ρ is the sparse target. In the training process, the sigmoid function is used as the activation function for each layer of the network.

Second, the calculation and optimization of J_{MMD} are described. Assume that X_s (which has m pieces of data), X_t (which has n pieces of data), $z_s^{l(i)}$, and $z_t^{l(i)}$ represent the source domain, target domain, output of the l th hidden layer of the i th sample in the source domain, and output of the l th hidden layer of the jth sample in the target domain, respectively.

Accordingly, the MMD-based probability distribution consistency constraint of the source and target domains in the l th hidden layer can be expressed as follows:

$$J_{\mathrm{MMD}}^{l}(\theta) = \mathrm{MMD}\left(Z_s^l, Z_t^l\right)^2 = \left\| \frac{1}{m}\sum_{i=1}^{m}\varphi\left(z_s^{l(i)}\right) - \frac{1}{n}\sum_{j=1}^{n}\varphi\left(z_t^{l(j)}\right) \right\|_{\mathscr{H}}^2, \tag{8}$$

where $\|\cdot\|_{\mathscr{H}}$ represents the normal RKHS form. Using the kernel trick, the above equation can be rewritten as

$$J_{\mathrm{MMD}}^{l}(\theta) = \mathrm{MMD}\left(Z_s^l, Z_t^l\right)^2 = \left\| \frac{1}{m}\sum_{i=1}^{m}\varphi\left(z_s^{l(i)}\right) - \frac{1}{n}\sum_{j=1}^{n}\varphi\left(z_t^{l(j)}\right) \right\|_{\mathscr{H}}^2$$
$$= \frac{1}{m^2}\sum_{i,j=1}^{m} K\left(z_s^{l(i)}, z_s^{l(j)}\right) - \frac{2}{mn}\sum_{i,j=1}^{m,n} K\left(z_s^{l(i)}, z_t^{l(j)}\right) + \frac{1}{n^2}\sum_{i,j=1}^{n} K\left(z_t^{l(i)}, z_t^{l(j)}\right). \tag{9}$$

The kernel function uses a Gaussian kernel, which is expressed as

$$K\left(z_s^{l(i)}, z_t^{l(j)}\right) = \exp\left(-\frac{\left\| z_s^{l(i)} - z_t^{l(j)} \right\|^2}{2\sigma^2}\right), \tag{10}$$

where σ is set equal to $\sqrt{d/2}$ [49] and d is the dimension of the output vector. Note that when updating the parameters (W_E^l, b_E^l, W_D^l, and b_D^l), only J_{MMD}^l is related to the encoding process. Therefore,

$$\frac{\partial J_{\mathrm{MMD}}^{l}}{\partial W_D^l} = 0, \frac{\partial J_{\mathrm{MMD}}^{l}}{\partial b_D^l} = 0,$$
$$\frac{\partial J_{\mathrm{MMD}}^{l}}{\partial W_E^l} = \frac{1}{m^2}\sum_{i,j=1}^{m}\frac{\partial K\left(z_s^{l(i)}, z_s^{l(j)}\right)}{\partial W_E^l} - \frac{2}{mn}\sum_{i,j=1}^{m,n}\frac{\partial K\left(z_s^{l(i)}, z_t^{l(j)}\right)}{\partial W_E^l} + \frac{1}{n^2}\sum_{i,j=1}^{n}\frac{\partial K\left(z_t^{l(i)}, z_t^{l(j)}\right)}{\partial W_E^l}, \tag{11}$$
$$\frac{\partial J_{\mathrm{MMD}}^{l}}{\partial b_E^l} = \frac{1}{m^2}\sum_{i,j=1}^{m}\frac{\partial K\left(z_s^{l(i)}, z_s^{l(j)}\right)}{\partial b_E^l} - \frac{2}{mn}\sum_{i,j=1}^{m,n}\frac{\partial K\left(z_s^{l(i)}, z_t^{l(j)}\right)}{\partial b_E^l} + \frac{1}{n^2}\sum_{i,j=1}^{n}\frac{\partial K\left(z_t^{l(i)}, z_t^{l(j)}\right)}{\partial b_E^l},$$

where $\partial K(z_s^{l(i)}, z_s^{l}(j))/\partial W_E^l$, $\partial K(z_s^{l(i)}, z_t^{l(j)})/\partial W_E^l$, $\partial K(z_t^{l(i)}, z_t^{l(j)})/\partial W_E^l$, $\partial K(z_s^{l(i)}, z_s^{l(j)})/\partial b_E^l$, $\partial K(z_s^{l(i)}, z_t^{l(j)})/\partial b_E^l$, and $\partial K(z_t^{l(i)}, z_t^{l(j)})/\partial b_E^l$ can be calculated according to the chain rule.

In the current unsupervised domain adaptation problem, the selection of hyperparameters remains a difficult problem. Moreover, unified and standard model parameter selection methods are not available. Therefore, in the model debugging process in this study, each parameter is selected within a certain range. The parameter selection process for the submodel DCS-DAE can be found in the research results by Cao et al. [31].

As discussed in Section 3.4.1, the parameter λ in equation (6) plays a crucial role in balancing the classification loss term and the domain discrepancy term. However, determining the optimal value of λ through validation is not feasible due to the absence of labels in the target domain within the model's framework [50]. To address this, the sensitivity of the parameter λ is explored and a recent approach for parameter selection in unsupervised domain adaptation called deep embedded validation [51] is examined. Figure 4 depicts the target intersection over union (IoU) for Task 4 in the target domain, with varying parameter λ. λ falls within the range of {1, 5, 10, 50, 100, 300, 500, 800, 1000}, allowing for a comprehensive investigation of its influence across a wide range of magnitudes. The results show that the IoU follows a bell-shaped curve, where it initially increases with λ, reaches its maximum at $\lambda = 1000$, and then decreases as λ decreases. This observation can be reasonably explained by the fact that a small λ causes the network to disregard domain discrepancies and focus solely on damage localization in the source domain, resulting in reduced IoU in the target domain. On the other hand, an excessively large λ leads to an emphasis on domain discrepancy loss, which ultimately impairs the network's ability to identify damage. In conclusion, achieving optimal performance in the target domain requires selecting an appropriate value for λ ($\lambda = 1000$), as both excessively small and excessively large values will result in a decrease in target IoU.

4. Numerical Simulation

4.1. Design of Source and Target Domains. In this study, to build the framework, a numerical model verified by experiments is used. This verification ensures the reliability of the model and is effective in testing the recognition effect of the algorithm on various scenarios of the arch dam. The Baihetan Dam is a large-span double-curvature arch dam that uses advanced technologies. The dam has a height of 289 m and is the largest hydropower station in the world; accordingly, it is selected as the research object. In the dynamic calculation, hydrodynamic pressure is applied to the nodes located on the upstream surface of the dam using the additional mass method proposed by Westergaard [52]. The concrete damaged plasticity (CDP) model proposed by Lee and Fenves [53] is adopted for the dam body. The sensor layout scheme is designed using the normal cloud mutation-shuffled frog leaping algorithm (NCM-SFLA) proposed by Cao et al. [54]. A sensor system consisting of 32 single-axis acceleration sensors (the test direction is along the river) is also integrated, as shown in Figure 5.

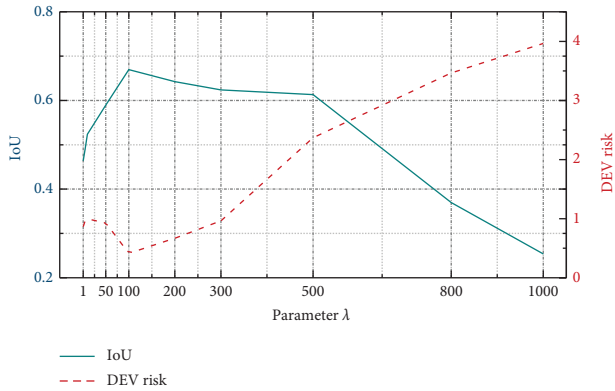

Figure 4: Target IoU and DEV risk with different λ in target domain 4.

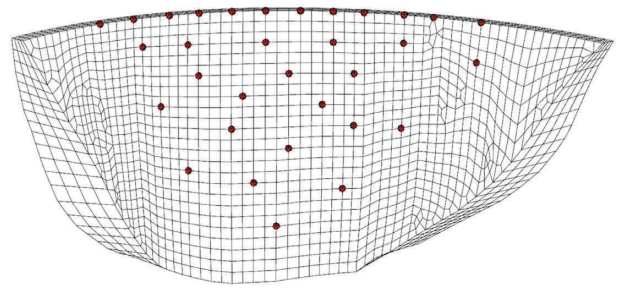

Figure 5: Sensor placement scheme determined by NCM-SFLA [54].

Four types of target domain models are designed by introducing random structural element stiffness and load variation disturbances considering different water levels. Then, different monitoring scenarios during the operation of the arch dam are reproduced. For the target domain data to be more consistent with the status of the actual project operation, the operation scenario of the Baihetan Arch Dam is described. The reservoir starts to store water near the dead water level (765 m) in June until the flood control limit level (785 m) is reached. The flood control limit water level was maintained from June to July. Every 10 d, the water level was controlled at 10 m from early August until the water level reached the normal water level (825 m) in early September. The reservoir supplied water from December to the end of May of the following year with water approximating the dead water level (765 m). Accordingly, the vibration data of the arch dam when the water level was normal were considered as the source domain. The vibration data when the water was at the flood control limit and dead water levels were selected for the two target domains. The number of samples in each target domain is half the number of samples in the source domain. This reproduces the state in which the amount of structural vibration data in some scenarios in actual engineering is low, as listed in Table 1. The following describes the working conditions of the four target domains.

4.1.1. Target Domain 1. The modeling error of the numerical model is reproduced considering the influence of the heterogeneity of dam material parameters on the vibration response signal owing to factors, such as zonal pouring. The Baihetan Arch Dam is partitioned according to the portioning method reported in [55], assigning different elastic moduli to various regions. The elastic moduli of materials in the same area may not be uniform during the pouring process. Hence, a slight disturbance is introduced according to the mean value of the elastic modulus of each area to simulate the state of the arch dam in actual engineering. Based on the random field simulation method of the spatial variability of structural materials [56, 57], the dynamic elastic modulus of each area of the arch dam is assumed to conform to a log-normal distribution with a certain mean and coefficient of variation [58]. To simplify the simulation process, autocorrelation distance is ignored. Finally, each element in every area obeys the following material parameter settings: the elastic modulus has a slight disturbance in its interval, and the density is uniform, as shown in Figure 6.

4.1.2. Target Domains 2 and 3. The interference of water level loading conditions is considered in these domains. Target domains 2 and 3 are the operating scenarios of the intact structure with uniform material distribution when the water heights are under the flood control limit (785 m) and dead water level (765 m) conditions, respectively.

4.1.3. Target Domain 4. The heterogeneity of material parameters and interference of water level load conditions are considered together to increase the gap between the source and target domains further. Therefore, target domain 4 represents the vibration data of the dam body at the dead

Table 1: Acquisition status of source and target domain data.

Scenario	Interference type	Brief description	Sample number
$\mathscr{D}_s$	None	Homogeneous/normal water level	120
$\mathscr{D}_t$ 1	Stiffness	Heterogeneous/normal water level	60
$\mathscr{D}_t$ 2	Water level	Homogeneous/flood control limit water level	60
$\mathscr{D}_t$ 3	Water level	Homogeneous/dead water level	60
$\mathscr{D}_t$ 4	Stiffness/water level	Heterogeneous/dead water level	60

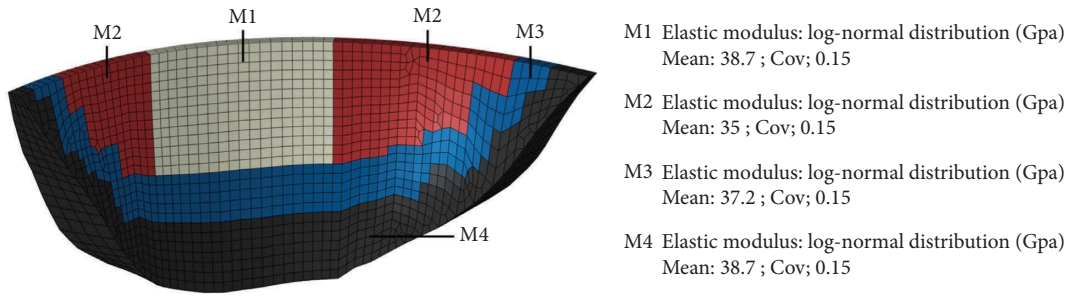

Figure 6: Schematic of arch dam partition and selection of random parameters.

water level (765 m), considering that the elastic modulus of each region conforms to the log-normal distribution.

4.2. Test Case Design. To simulate the damage to an arch dam, typically, the structure is first divided into zones and then the elastic modulus of each zone is reduced to a fixed value. However, during an earthquake, the damage to each part of the dam is related, and the traditional damage simulation method conceals the actual damage state. Therefore, the equivalent damage model for high arch dams subjected to earthquakes proposed by Chen et al. [59] was adopted in this study. The advantage of this model is that it can rapidly reverse damage without losing the damage correlation among various parts of the dam body. The derivation and experimental verification of this model are discussed in detail in the literature [59, 60], as shown in Figures 7(a)–7(c). Three values of stiffness reduction (20%, 50%, and 80%) are specified for the damage center on the downstream face of the dam body. They are expanded in a certain ellipsoidal space to design an intact scenario (IS) and three damage scenarios (DSs), as shown in Figures 7(d)–7(f).

The following five types of test samples are set according to the design principle of the target domain: source domain (S), $\mathscr{D}_t$ 1 (T1), $\mathscr{D}_t$ 2 (T2), $\mathscr{D}_t$ 3 (T3), and $\mathscr{D}_t$ 4 (T4). Each type of test sample is divided into four levels (IS, DS1, DS2, and DS3). Twenty test scenarios are listed in Table 2; S-S indicates that the training set is only composed of the data generated by the benchmark model. The training data, S-T1–S-T4, are composed of those generated by the benchmark model and four revised models. To obtain the vibration information of the arch dam in an actual engineering scene as soon as possible, a multifrequency sine wave with added noise is used as excitation load [23], as shown in Figure 8. The sampling time for each calculation is 5 s, and the sampling frequency is 200 Hz. Each scene model of the arch dam is calculated 180 and 30 times under intact and damaged conditions, respectively.

4.3. Influence of Model Error on Natural Frequency of Structure. Wet modal analysis was performed on each domain case to explore the differences among the four target domains relative to the source domain. Table 3 summarizes the first five natural frequencies corresponding to each wet mode of the target domain as well as the frequency difference between the target and source domain models. The table indicates that the model gap between target domain 1 and the source domain is small. This is because the setting of target domain 1 does not consider the autocorrelation distance of material spatial differences. Although the elastic mode of the material is spatially nonuniform, because the positive and negative disturbances nullify each other, the entire material conforms to the log-normal distribution. The difference between the source domain and target domains 2 and 3 is considerable, indicating that the change in operating water level has a significant influence on the dynamic response of the arch dam. The gap between target domain 4 and the source domain model is the largest among all domain cases. This is because target domain 4 simultaneously considers the effects of material inhomogeneity and water level changes. Notably, the related results [31] indicate that the spatial randomness of the material has a negligible effect on the mean of the response of each area of the structure; however, the standard deviation of the spatial distribution is considerable. Therefore, the effect of material randomness on the structure cannot be accurately measured based merely on the mode shape. This effect can be more directly reflected by the standard deviation of the responses.

4.4. Data Preprocessing and Evaluation Criteria. In a real environment, noise is typically caused by many different sources. Real noise is assumed to be a combination of many random variables with different probability distributions; each variable is presumed independent. Then, according to

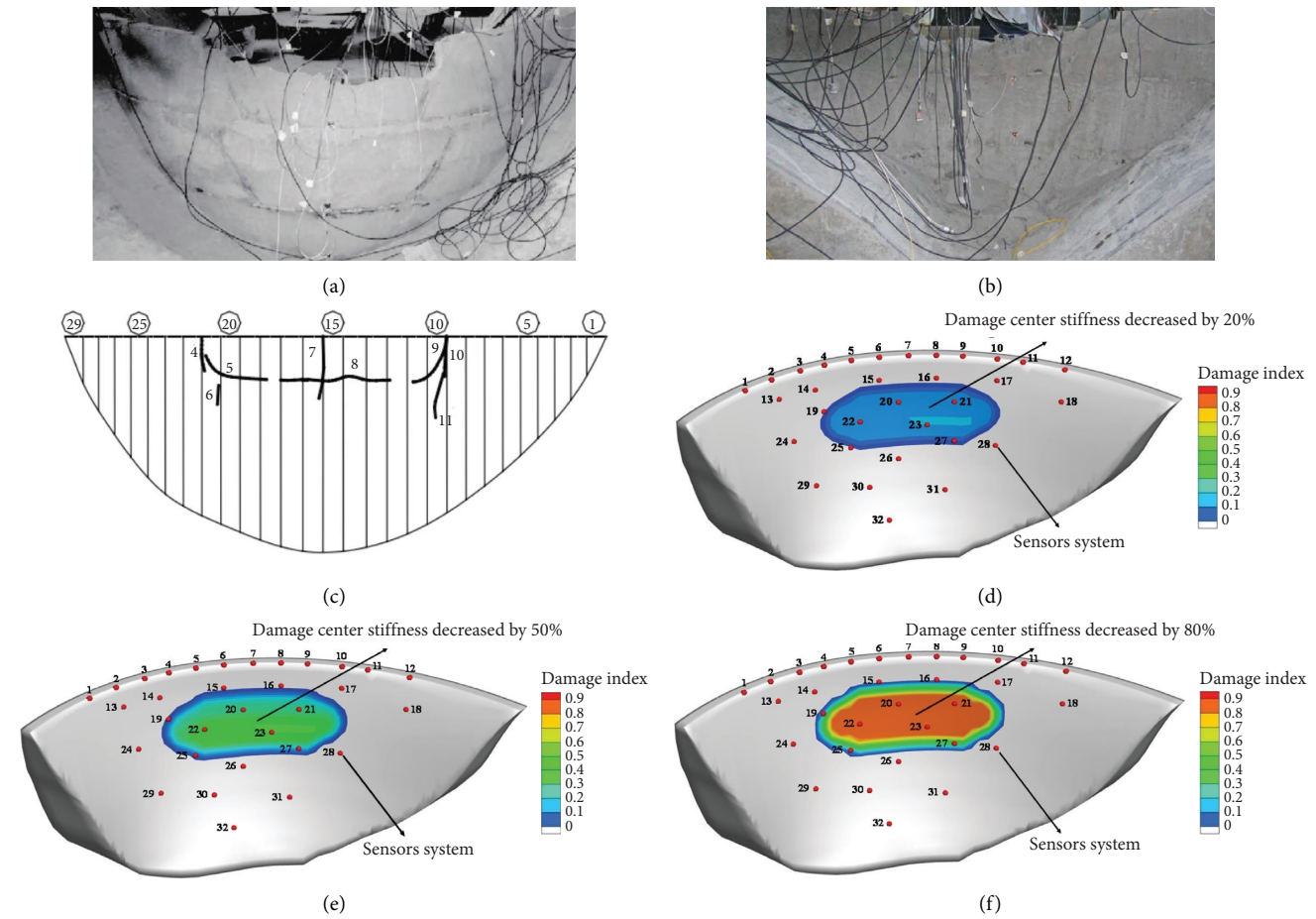

Figure 7: Equivalent damage model of high arch dams subjected to earthquakes and test verification. (a) Failure form of upstream face of high arch dam in shaking table test. (b) Failure mode of downstream face of high arch dam in shaking table test. (c) Main failure path of downstream surface. (d) DS 1: stiffness of damage center decreases by 20%. (e) DS 2: stiffness of damage center decreases by 50%. (f) DS 3: stiffness of damage center decreases by 80%.

Table 2: Design of test sample conditions.

$\mathscr{D}_s$-$\mathscr{D}_t$	Code	Brief description	Sample number
S-S	S-IS	Material is homogeneous in space	180
	S-DS 1	Water is at dead water level (765 m)	30
	S-DS 2	Stiffness of damage center decreases by 0%, 20%, 50%, and 80%	30
	S-DS 3		30
S-T1	T1-IS	Material is homogeneous in space	180
	T1-DS 1	Water is at dead water level (765 m)	30
	T1-DS 2	Stiffness of damage center decreases by 0%, 20%, 50%, and 80%	30
	T1-DS 3		30
S-T2	T2-IS	Material is homogeneous in space	180
	T2-DS 1	Water is at dead water level (765 m)	30
	T2-DS 2	Stiffness of damage center decreases by 0%, 20%, 50%, and 80%	30
	T2-DS 3		30
S-T3	T3-IS	Material is homogeneous in space	180
	T3-DS 1	Water is at dead water level (765 m)	30
	T3-DS 2	Stiffness of damage center decreases by 0%, 20%, 50%, and 80%	30
	T3-DS 3		30
S-T4	T4-IS	Elastic modulus obeys log-normal distribution	180
	T4-DS 1	Water is at dead water level (765 m)	30
	T4-DS 2	Stiffness of damage center decreases by 0%, 20%, 50%, and 80%	30
	T4-DS 3		30

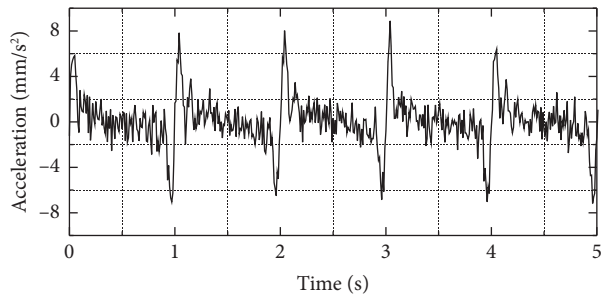

Figure 8: Wave components of multifrequency sinusoidal wave excitation with Gaussian white noise.

Table 3: Model error and wet modal analysis results of structure under different operating states.

Scenario	1st mode		2nd mode		3rd mode		4th mode		5th mode	
	Frequency (Hz)	ERR (%)	Frequency (Hz)	ERR (%)	Frequency (Hz)	ERR (%)	Frequency (Hz)	ERR (%)	Frequency (Hz)	ERR (%)
$\mathscr{D}_s$	1.1317	—	1.3004	—	1.9173	—	2.2429	—	2.5770	—
$\mathscr{D}_t$ 1	1.1794	4.21	1.3540	4.12	1.9989	4.26	2.3423	4.43	2.6870	4.38
$\mathscr{D}_t$ 2	1.3130	16.02	1.4683	12.91	2.1846	13.94	2.5368	13.10	2.9035	12.67
$\mathscr{D}_t$ 3	1.3889	22.72	1.5324	17.84	2.2702	18.41	2.6106	16.39	3.0040	16.57
$\mathscr{D}_t$ 4	1.4452	27.70	1.5931	22.51	2.3650	23.35	2.7265	21.56	3.1291	21.42

the central limit theorem, their normalized sum tends toward a Gaussian distribution with an increase in the number of noise sources. Therefore, to test the resistance of the proposed method to noise, the acceleration signals collected under each test condition are polluted with Gaussian white noise with a signal-to-noise ratio of 4 dB. Before inputting the original acceleration response signal measured in the time dimension into the model for data reconstruction, the input data must be normalized. This ensures that the data of each indicator are of the same order of magnitude, thus eliminating the dimensional influence on the indicators. In this study, the Z-score method was applied to normalize the acceleration response signals measured by each sensor, and $1.5 \times \mathrm{IQR}$ [61–64] was used as the threshold for abnormal warning. An appropriate discrimination index plays an important role in the reliability of model discrimination. The confusion matrix can evaluate the model from different levels, as shown in Figure 9.

In order to comprehensively consider the evaluation effects of precision and recall, F-score is introduced as a model evaluation method. F-score is the harmonic mean of precision and recall, which can be given by

$$F - \text{score} = \left(1 + \beta^2\right) \times \frac{\text{precision} \times \text{recall}}{\beta^2 \cdot \text{precision} + \text{recall}} \times 100\%. \tag{12}$$

The damage identification method in this paper considers that precision and recall are equally important, so $F1$ score ($\beta = 1$) is chosen as the evaluation metric for the model's performance [65]. In addition, in order to comprehensively consider all false positives and false negatives, mean intersection over union (MIoU) is introduced as model evaluation index, which can be given by

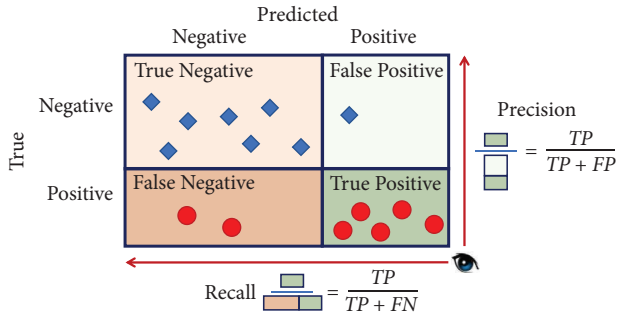

Figure 9: Graphic confusion matrix.

$$\mathrm{MIoU} = \frac{1}{k+1} \sum_{i=0}^{k} \frac{p_{ii}}{\sum_{j=0}^{k} p_{ji} + \sum_{j=0}^{k} p_{ij} - p_{ii}}, \tag{13}$$

where $k+1$ represents k foreground classes and 1 background class, p_{ii} represents the number of pixels correctly classified, p_{ij} represents the number of pixels of class i predicted as class j, and p_{ji} represents the number of pixels of class j predicted as class i. The range of MIoU is from 0 to 1, and a higher value indicates better performance of the model.

Note that the core of the proposed method is information reconstruction, and the cross-domain may lead to a reduction in the reconstruction ability of the model. In other words, the model, which is constructed using the source domain data only, considerably enhances the detection of abnormal samples in other domains but significantly weakens the model's ability to identify normal samples. To highlight the ability of the model to detect normal samples, the number of normal samples in each domain was designed to be twice the sum of the number of

abnormal samples of different degrees ($2 \times (30 + 30 + 30) = 180$).

4.5. Analysis Results. The training time for the damage identification is approximately 127 to 136 min in a Python 3.8 environment. The abnormal diagnosis capability of the DCS-DAE model without introducing domain adaptive technology to each test condition is shown in Figure 10(a). The $F1$ score obtained by DCS-DAE in the source domain model is as high as 95.51%. Hence, the model has good diagnostic ability under various damage conditions in this domain. However, the anomaly detection model constructed using source and target domain data also had a considerably high recall value for abnormal samples. In contrast, the recall value for the intact samples of other target domains significantly decreased.

In other words, if the data in the source and target domains are concurrently used as training samples, differentiating between intact and abnormal samples can be easier; the network is constructed through the DCS-DAE model without introducing domain adaptation. Thus, the ability to identify different damage conditions in each domain cannot be used as the standard for the successful migration of the model; instead, the ability of the model to identify intact samples must be considered. The use of $F1$ score can resolve this problem to a certain extent. As expected, the $F1$ score obtained by the DCS-DAE in the source domain model was as high as 95.51%; however, the $F1$ score decreased to varying degrees during anomaly detection in other domains.

The current DCS-DAE model has a considerably high recall value for the diagnosis of abnormal samples in each domain; Figure 10(b) shows the degradation of the model performance caused by the cross-domain. In target domain 1, as a result of perturbing the stiffness of the structural model, the $F1$ score and recall value for identifying intact samples are only attenuated by 2.38% and 4.44%, respectively. This shows that the complete randomness of material space within a certain range has negligible discreteness in the overall response.

In target domain 2, the level of water impounded by the dam is reduced to the flood control limit (785 m), which is 40 m lower than that in the source domain. As expected, the $F1$ score of the DCS-DAE model for recognizing abnormal samples is only 68.44%. The performance and recall values of recognizing normal samples decrease by 27.06% and 44.44%, respectively, compared with those of recognizing samples in the source domain. This phenomenon confirms that the structural features extracted by the DCS-DAE model are related to the water level. In target domain 3, water impounded by the dam is further reduced to the dead water level (765 m), which is 60 m lower than that in the source domain. The $F1$ score of abnormal sample recognition and the recall value of normal sample recognition are further reduced. The extent of attenuation is 36.09% and 66.67%, respectively, compared with that of the source domain. In target domain 4, the $F1$ score of abnormal samples identified by the model is only 57.88%. The attenuation degree of the $F1$ score for abnormal sample recognition and the recall value of normal sample recognition are 37.63% and 71.11%, respectively, compared with those of recognizing samples in the source domain. Moreover, the IoU of the DCS-DAE without domain adaptation model corresponding to source domain and target domain 1 to target domain 4 is 0.91, 0.87, 0.52, 0.42, and 0.40, respectively. The MIoU of this model is only 0.55. The foregoing discussion shows that the anomaly detection model using the DCS-DAE without domain adaptation has certain limitations. In other words, the training data must virtually be in the same scene, and the detection scene must be consistent with the training scene during application. To a certain extent, this restricts the implementation of damage identification based on feature extraction in practical engineering.

The convergence curve of the MMD values of the DCS-DAE model with domain adaptation in the four target domains during the training process is shown in Figure 11. The trend of the MMD value change curve is similar in each target domain. Specifically, MMD values start from zero because at the beginning of training, the weights and offsets in the network are randomly set, resulting in a random output. At this stage, the network cannot extract the characteristics of the source and target domains; consequently, the gap between the two cannot be reflected. With an increase in training time, the corresponding MMD values of each target domain improve. This is because the main goal of the network at this stage is to extract features reflecting the structural health state to the extent possible (i.e., in the trial learning stage). Next, the MMD value gradually decreased because the network gradually extracted the common domain features of the structure corresponding to different water levels. That is, a set of parameters that gradually render the characteristics of the source and target domain data sufficiently similar to achieve the purpose of migration is found. In general, when the MMD value is stable, its convergence values, arranged from high to low, are those from target domains 4, 3, 2, and 1. This is consistent with the detection performance attenuation of DCS-DAE without adaptation in the target domain, as shown in Figure 10(b); the greater the model error, the higher the MMD value at the time of convergence.

The diagnostic capability of the DCS-DAE model based on domain adaptation in the four target domains is shown in Figure 12(a). The performance difference between the DCS-DAE model (with domain adaptation) and traditional DCS-DAE model (under various evaluation criteria) is presented in Figure 12(b). The figure indicates that after introducing domain adaptation, the $F1$ score, from target domain 1 to target domain 4, improves by 1.38%, 18.33%, 24.27%, and 22.33%, respectively. This shows that the DCS-DAE model with domain adaptation has improved the $F1$ scores of all target domains. This improvement is more evident with increasing environmental load and model gap. In addition, after introducing the domain-adaptive method, the recall values of the intact structure considering those from target domain 1 to target domain 4 increase by 2.78%, 36.67%, 55.00%, and 57.22%, respectively. In

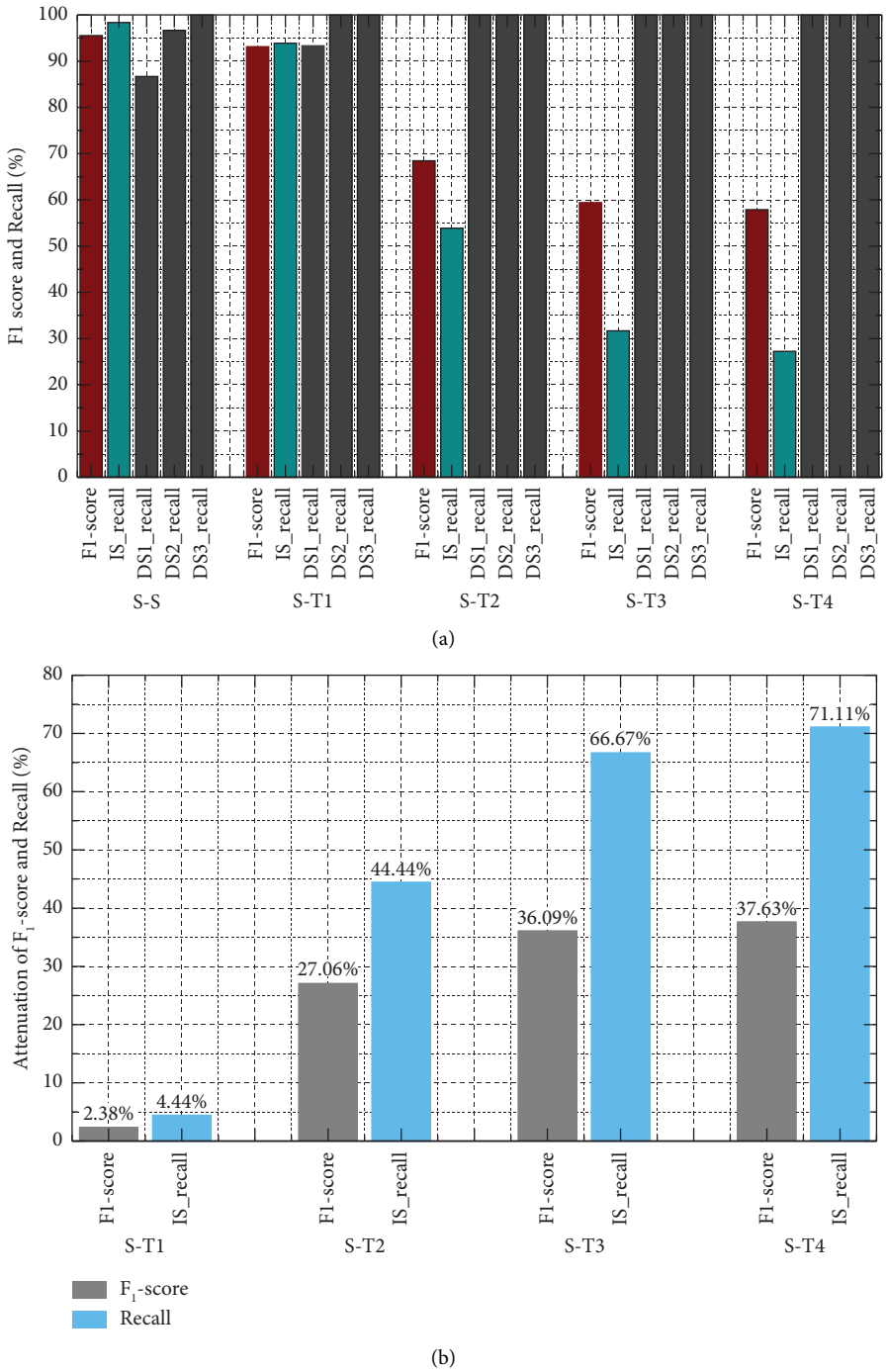

FIGURE 10: Performance of DCS-DAE without domain adaptation under different test conditions. (a) Recognition performance of DCS-DAE model without adaptation in each domain. (b) Performance degradation caused by cross-domain.

contrast, the recall value under each damage condition only slightly increased. The IoU of DCS-DAE with domain adaptation model corresponding to source domain and target domain 1 to target domain 4 is 0.94, 0.90, 0.77, 0.72 and 0.70, respectively. The MIoU of this model is 0.81, which is 0.19 higher than that of the model without domain adaptation. Accordingly, the DCS-DAE model based on domain adaptation can effectively reduce the distribution difference between the high-dimensional features of the source and target domain data. Consequently, the model can simultaneously extract features with a more robust structure from a considerable amount of source domain data and a small amount of target domain data.

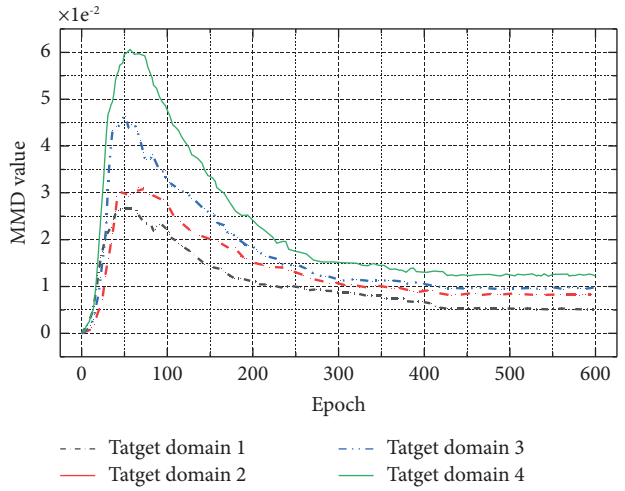

Figure 11: Convergence curve of MMD value during training.

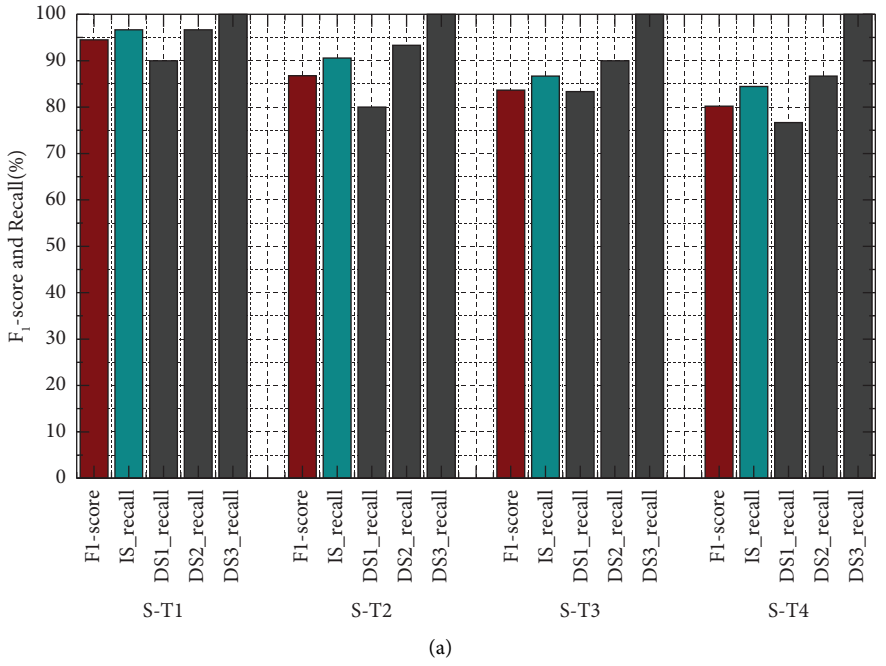

(a)

Figure 12: Continued.

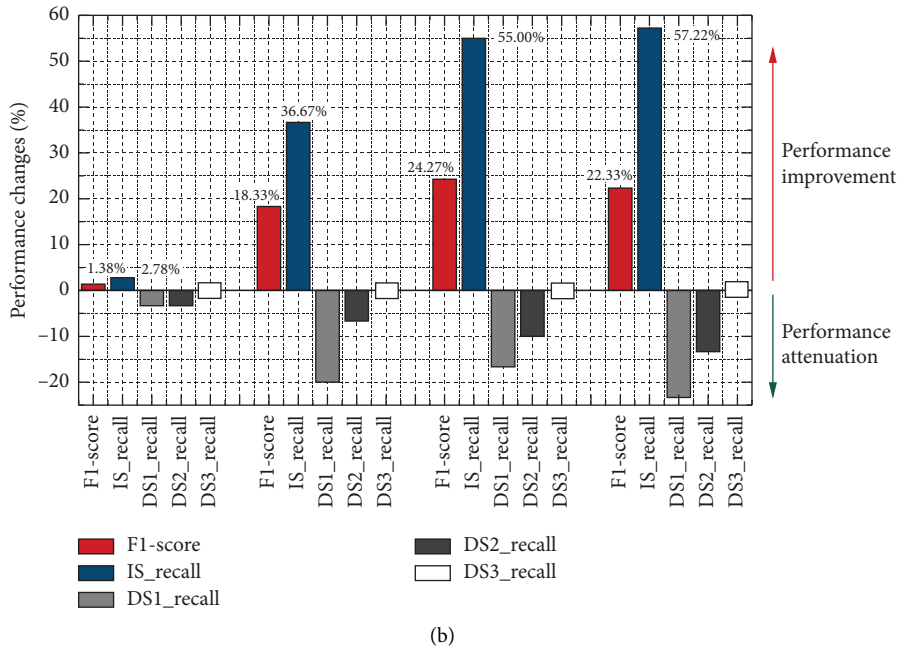

(b)

Figure 12: Performance of DCS-DAE model based on domain adaptation under different conditions. (a) Recognition performance of DCS-DAE model based on adaptation in each domain. (b) Performance improvement by introducing domain adaptation.

5. Discussion and Conclusion

In this study, a DCS-DAE model based on domain adaptation is proposed considering the anomaly detection requirements of arch dams under different water level conditions in actual engineering scenarios. The main findings are as follows:

(1) The anomaly detection method based on the unsupervised learning model of DCS-DAE has a high limit on test conditions, restricting the application of this method to actual arch dam project scenarios. When the water level conditions in the test scenario differ from those in the training scenario, the anomaly detection capability in the test scenario is significantly reduced. The greater the difference between the water level conditions of the test and training scenarios, the worse the anomaly detection performance of the DCS-DAE model.

(2) Based on the traditional DCS-DAE model, a novel DCS-DAE model that uses domain adaptation is constructed by introducing the MMD criterion in the loss function of parameter optimization. Four target domains are constructed using the equivalent damage model of high arch dams subjected to earthquakes. The results show that the $F1$ scores of the DCS-DAE model based on domain adaptation in the four target domains compared with those of the traditional DCS-DAE model increased by 1.38%, 18.33%, 24.27%, and 22.33%, respectively. The MIoU of the proposed model is 0.81, which is 0.19 higher than that of the model without domain adaptation. In general, the DCS-DAE model based on domain adaptation technology significantly improves the generalization and robustness of features obtained from the data in different scenarios.

(3) The impact of environmental loads and modeling errors on the source domain model can be effectively measured by MMD. The performance attenuation of the DCS-DAE model without domain adaptation in each target domain is positively correlated with the MMD value in each target domain; the higher the MMD value, the lower the anomaly detection performance. Moreover, in the training of the DCS-DAE model based on domain adaptation, with a decrease in the MMD value, the performance of anomaly detection gradually improves. Therefore, in practical engineering, the influence of environmental load or model error on structural anomaly detection can be determined according to the MMD value.

Data Availability

No data were used to support this study.

Conflicts of Interest

The authors declare that they have no conflicts of interest.

Authors' Contributions

Xiangyu Cao was responsible for methodology, data curation, software, original draft preparation, and funding acquisition. Liang Chen was responsible for conceptualization, data curation, and draft revision. Jianyun Chen was responsible for conceptualization, supervision, funding acquisition, and project administration. Jing Li was responsible for investigation, methodology, and data curation. Wenyan

Lu was responsible for conceptualization, methodology, and software. Haixiang Liu was responsible for conceptualization, supervision, and review and editing. Pengfei Liu was responsible for methodology, software, and draft revision. Minyong Ke was responsible for formal analysis, visualization, and original draft preparation. Yunqing Tang was responsible for conceptualization, funding acquisition, and project administration.

Acknowledgments

The authors are grateful for the joint support of the National Natural Science Foundation of China (grant no. 52079025), the National Key R&D Program of China (grant no. 2020YFC1511905), the Natural Science Foundation of Jiangsu Province (grant no. BK20220206), and the Central Public-Interest Scientific Institution Basal Research Fund of China (grant no. Y422003).

References

[1] Y. J. Cha, W. Choi, G. Suh, S. Mahmoudkhani, and O. Buyukozturk, "Autonomous structural visual inspection using region-based deep learning for detecting multiple damage types," *Computer-Aided Civil and Infrastructure Engineering*, vol. 33, no. 9, pp. 731–747, 2018.

[2] D. H. Kang and Y. J. Cha, "Autonomous UAVs for structural health monitoring using deep learning and an ultrasonic beacon system with geo-tagging," *Computer-Aided Civil and Infrastructure Engineering*, vol. 33, no. 10, pp. 885–902, 2018.

[3] S. J. Xu, M. Hao, G. H. Liu, Y. B. Meng, J. Q. Han, and Y. Q. Shi, "Concrete crack segmentation based on convolution-deconvolution feature fusion with holistically nested networks," *Structural Control and Health Monitoring*, vol. 29, no. 8, 2022.

[4] Y. J. Cha, W. Choi, and O. Buyukozturk, "Deep learning-based crack damage detection using convolutional neural networks," *Computer-Aided Civil and Infrastructure Engineering*, vol. 32, no. 5, pp. 361–378, 2017.

[5] X. W. Ye, S. Y. Ma, Z. X. Liu, Y. Ding, Z. X. Li, and T. Jin, "Post-earthquake damage recognition and condition assessment of bridges using UAV integrated with deep learning approach," *Structural Control and Health Monitoring*, vol. 29, no. 12, 2022.

[6] S. C. Kuok, K. V. Yuen, S. Roberts, and M. A. Girolami, "Propagative broad learning for nonparametric modeling of ambient effects on structural health indicators," *Structural Health Monitoring*, vol. 20, no. 4, pp. 1409–1427, 2020.

[7] A. Entezami, H. Sarmadi, B. Behkamal, and S. Mariani, "Big data analytics and structural health monitoring: a statistical pattern recognition-based approach," *Sensors*, vol. 20, no. 8, p. 2328, 2020.

[8] H. B. Huang, T. H. Yi, and H. N. Li, "Anomaly identification of structural health monitoring data using dynamic independent component analysis," *Journal of Computing in Civil Engineering*, vol. 34, no. 5, 2020.

[9] A. Entezami, H. Shariatmadar, and A. Karamodin, "Data-driven damage diagnosis under environmental and operational variability by novel statistical pattern recognition methods," *Structural Health Monitoring*, vol. 18, no. 5-6, pp. 1416–1443, 2018.

[10] S. Zheng, C. F. Shao, C. S. Gu, and Y. X. Xu, "An automatic data process line identification method for dam safety monitoring data outlier detection," *Structural Control and Health Monitoring*, vol. 29, no. 7, 2022.

[11] W. Zhang, Z. W. Wang, and X. Li, "Reliability engineering and system safety," *Blockchain-based decentralized federated transfer learning methodology for collaborative machinery fault diagnosis*, vol. 229, 2023.

[12] X. Li, Y. X. Xu, N. P. Li, B. Yang, and Y. G. Lei, "Remaining useful life prediction with partial sensor malfunctions using deep adversarial networks," *IEEE/CAA Journal of Automatica Sinica*, vol. 10, no. 1, pp. 121–134, 2023.

[13] X. Wu, D. J. Zheng, Y. T. Liu, Z. Y. Chen, and X. Q. Chen, "Temporal convolution network-based time frequency domain integrated model of multiple arch dam deformation and quantification of the load impact," *Structural Control and Health Monitoring*, vol. 29, no. 11, 2022.

[14] Y. Kankanamge, Y. F. Hu, and X. Y. Shao, "Application of wavelet transform in structural health monitoring," *Earthquake Engineering and Engineering Vibration*, vol. 19, no. 2, pp. 515–532, 2020.

[15] T. H. Yi, H. B. Huang, and H. N. Li, "Development of sensor validation methodologies for structural health monitoring: a comprehensive review," *Measurement*, vol. 109, pp. 200–214, 2017.

[16] H. B. Huang, T. H. Yi, and H. N. Li, "Canonical correlation analysis based fault diagnosis method for structural monitoring sensor networks," *Smart Structures and Systems*, vol. 17, no. 6, pp. 1031–1053, 2016.

[17] F. T. Ni, J. Zhang, and M. N. Noori, "Deep learning for data anomaly detection and data compression of a long-span suspension bridge," *Computer-Aided Civil and Infrastructure Engineering*, vol. 35, no. 7, pp. 685–700, 2020.

[18] Z. L. Wang and Y. J. Cha, "Automated Damage-Sensitive Feature Extraction Using Unsupervised Convolutional Neural Networks," *Conference On Sensors And Smart Structures Technologies For Civil, Mechanical, and Aerospace Systems*, 2018.

[19] Y. J. Xu, X. Z. Lu, B. Cetiner, and E. Taciroglu, "Real-time regional seismic damage assessment framework based on long short-term memory neural network," *Computer-Aided Civil and Infrastructure Engineering*, vol. 36, no. 4, pp. 504–521, 2020.

[20] C. S. N. Pathirage, J. Li, L. Li, H. Hao, W. Q. Liu, and P. H. Ni, "Structural damage identification based on autoencoder neural networks and deep learning," *Engineering Structures*, vol. 172, pp. 13–28, 2018.

[21] X. R. Ma, Y. Z. Lin, Z. H. Nie, and H. W. Ma, "Structural damage identification based on unsupervised feature-extraction via Variational Auto-encoder," *Measurement*, vol. 160, 2020.

[22] M. Azimi and G. Pekcan, "Structural health monitoring using extremely compressed data through deep learning," *Computer-Aided Civil and Infrastructure Engineering*, vol. 35, no. 6, pp. 597–614, 2020.

[23] Z. L. Wang and Y. J. Cha, "Unsupervised deep learning approach using a deep auto-encoder with a one-class support vector machine to detect damage," *Structural Health Monitoring*, vol. 20, no. 1, pp. 406–425, 2020.

[24] H. Sarmadi, "Investigation of machine learning methods for structural safety assessment under variability in data comparative studies and new approaches," *Journal of Performance of Constructed Facilities*, vol. 35, no. 6, 2021.

[25] Y. Y. Zhang, X. Y. Li, L. Gao, and P. G. Li, "A new subset based deep feature learning method for intelligent fault diagnosis of bearing," *Expert Systems with Applications*, vol. 110, pp. 125–142, 2018.

[26] Y. Z. Lin, Z. H. Nie, and H. W. Ma, "Structural damage detection with automatic feature-extraction through deep learning," *Computer-Aided Civil and Infrastructure Engineering*, vol. 32, no. 12, pp. 1025–1046, 2017.

[27] L. A. Bull, K. Worden, and N. Dervilis, "Towards semi-supervised and probabilistic classification in structural health monitoring," *Mechanical Systems and Signal Processing*, vol. 140, 2020.

[28] H. Sarmadi and K. V. Yuen, "Early damage detection by an innovative unsupervised learning method based on kernel null space and peak-over-threshold," *Computer-Aided Civil and Infrastructure Engineering*, vol. 36, no. 9, pp. 1150–1167, 2021.

[29] M. H. Soleimani Babakamali, R. Sepasdar, K. Nasrollahzadeh, I. Lourentzou, and R. Sarlo, "Toward a general unsupervised novelty detection framework in structural health monitoring," *Computer-Aided Civil and Infrastructure Engineering*, vol. 37, no. 9, pp. 1128–1145, 2022.

[30] Y. J. Cha and Z. L. Wang, "Unsupervised novelty detection-based structural damage localization using a density peaks-based fast clustering algorithm," *Structural Health Monitoring*, vol. 17, no. 2, pp. 313–324, 2018.

[31] X. Y. Cao, L. Chen, J. Y. Chen et al., "Seismic damage identification of high arch dams based on an unsupervised deep learning approach," *Soil Dynamics and Earthquake Engineering*, vol. 168, 2023.

[32] W. J. Sun, S. Y. Shao, R. Zhao, R. Q. Yan, X. W. Zhang, and X. F. Chen, "A sparse auto-encoder-based deep neural network approach for induction motor faults classification," *Measurement*, vol. 89, pp. 171–178, 2016.

[33] F. Jia, Y. G. Lei, J. Lin, X. Zhou, and N. Lu, "Deep neural networks: a promising tool for fault characteristic mining and intelligent diagnosis of rotating machinery with massive data," *Mechanical Systems and Signal Processing*, vol. 72-73, pp. 303–315, 2016.

[34] C. S. N. Pathirage, J. Li, L. Li, H. Hao, and W. Q. Liu, "Application of deep autoencoder model for structural condition monitoring," *Journal of Systems Engineering and Electronics*, vol. 29, no. 4, pp. 873–880, 2018.

[35] T. Hofmann, "Unsupervised learning by probabilistic latent semantic analysis," *Machine Learning*, vol. 42, no. 1/2, pp. 177–196, 2001.

[36] M. H. Rafiei and H. Adeli, "A novel unsupervised deep learning model for global and local health condition assessment of structures," *Engineering Structures*, vol. 156, pp. 598–607, 2018.

[37] M. D. Sun, H. Wang, P. Liu, S. D. Huang, and P. Fan, "A sparse stacked denoising autoencoder with optimized transfer learning applied to the fault diagnosis of rolling bearings," *Measurement*, vol. 146, pp. 305–314, 2019.

[38] S. J. Pan and Q. Yang, "A survey on transfer learning," *IEEE Transactions on Knowledge and Data Engineering*, vol. 22, no. 10, pp. 1345–1359, 2010.

[39] O. Day and T. M. Khoshgoftaar, "A survey on heterogeneous transferlearning," *Journal of Big Data*, vol. 4, no. 1, 2017.

[40] X. Chai, Q. S. Wang, Y. P. Zhao, X. Liu, O. Bai, and Y. Q. Li, "Unsupervised domain adaptation techniques based on auto-encoder for non-stationary EEG-based emotion recognition," *Computers in Biology and Medicine*, vol. 79, pp. 205–214, 2016.

[41] A. Gretton, K. Borgwardt, M. Rasch, B. Scholkopf, and A. J. Smola, "A kernel method for the two-sample-problem," *Advances in Neural Information Processing Systems*, vol. 19, pp. 513–520, 2006.

[42] C. Li, S. H. Zhang, Y. Qin, and E. Estupinan, "A systematic review of deep transfer learning for machinery fault diagnosis," *Neurocomputing*, vol. 407, pp. 121–135, 2020.

[43] K. M. Borgwardt, A. Gretton, M. J. Rasch, H. P. Kriegel, B. Scholkopf, and A. J. Smola, "Integrating structured biological data by kernel maximum mean discrepancy," *Bioinformatics*, vol. 22, no. 14, pp. 49–57, 2006.

[44] A. Gretton, B. Sriperumbudur, D. Sejdinovic et al., "Optimal kernel choice for large-scale two-sample tests," *Advances in Neural Information Processing Systems*, vol. 25, pp. 1205–1213, 2012.

[45] Y. Y. Zhang, X. Y. Li, L. Gao, W. Chen, and P. G. Li, "Ensemble deep contractive auto-encoders for intelligent fault diagnosis of machines under noisy environment," *Knowledge-Based Systems*, vol. 196, 2020.

[46] M. Abubaker, "Data mining applications in understanding electricity consumers' behavior: a case study of Tulkarm district, Palestine," *Energies*, vol. 12, no. 22, p. 4287, 2019.

[47] M. Vaghefi, K. Mahmoodi, and M. Akbari, "Detection of outlier in 3D flow velocity collection in an open-channel bend using various data mining techniques," *Iranian Journal of Science and Technology, Transactions of Civil Engineering*, vol. 43, no. 2, pp. 197–214, 2019.

[48] Y. Lei, C. H. Yan, S. Renu, A. Belay, and Y. S. Ye, "A modified WKNN indoor Wi-Fi localization method with differential coordinates," in *Proceedings of the International Conference on Applied System Innovation (ICASI)*, pp. 1822–1824, Sapporo, Japan, January 2017.

[49] B. Schölkopf, A. J. Smola, and F. Bach, *Learning with Kernels: Support Vector Machines, Regularization, Optimization, and beyond*, MIT press, 2001.

[50] Y. Z. Lin, Z. H. Nie, and H. W. Ma, "Dynamics-based cross-domain structural damage detection through deep transfer learning," *Computer-Aided Civil and Infrastructure Engineering*, vol. 37, no. 1, pp. 24–54, 2022.

[51] K. C. You, X. M. Wang, M. S. Long, and M. I. Jordan, "Towards Accurate Model Selection in Deep Unsupervised Domain Adaptation," in *Proceedings of the International Conference On Machine Learning*, pp. 7124–7133, Long Beach Convention and Entertainment Center, Long Beach, CA, USA, June 2019.

[52] H. M. Westergaard, "Water pressures on dams during earthquakes," *Transactions of the American Society of Civil Engineers*, vol. 98, no. 2, pp. 418–433, 1933.

[53] J. Lee and G. L. Fenves, "A plastic-damage concrete model for earthquake analysis of dams," *Earthquake Engineering & Structural Dynamics*, vol. 27, no. 9, pp. 937–956, 1998.

[54] X. Y. Cao, J. Y. Chen, Q. Xu, and J. Li, "A distance coefficient-multi objective information fusion algorithm for optimal sensor placement in structural health monitoring," *Advances in Structural Engineering*, vol. 24, no. 4, pp. 718–732, 2021.

[55] C. Liang, J. Y. Chen, Q. Xu, and J. Li, "Correlation study between seismic intensity measures and nonlinear response of arch dam via endurance time analysis," *KSCE Journal of Civil Engineering*, vol. 25, no. 1, pp. 256–271, 2020.

[56] J. Y. Chen, P. F. Liu, Q. Xu, and J. Li, "Seismic analysis of hardfill dams considering spatial variability of material parameters," *Engineering Structures*, vol. 211, 2020.

[57] X. Lu, Z. Y. Wu, L. Pei et al., "Effect of the spatial variability of strength parameters on the dynamic damage characteristics of gravity dams," *Engineering Structures*, vol. 183, pp. 281–289, 2019.

[58] V. E. Saouma, M. A. Hariri-Ardebili, and L. Graham-Brady, "Stochastic analysis of concrete dams with alkali aggregate reaction," *Cement and Concrete Research*, vol. 132, 2020.

[59] J. Chen, X. Cao, Q. Xu, and J. Li, "Exploration on damage mechanism and equivalent damage model of high arch dams

under earthquakes," *KSCE Journal of Civil Engineering*, vol. 24, no. 4, pp. 1285–1306, 2020.

[60] S. L. Fan, J. Y. Chen, J. Y. Wang, and H. Zhong, "Experimental study and numerical simulation for seismic failure of high arch dam on shaking table," *Chinese Journal of Rock Mechanics and Engineering*, vol. 28, no. 3, pp. 467–474, 2009.

[61] K. Carling, "Resistant outlier rules and the non-Gaussian case," *Computational Statistics & Data Analysis*, vol. 33, no. 3, pp. 249–258, 2000.

[62] M. Frigge, D. C. Hoaglin, and B. Iglewicz, "Some implementations of the boxplot," *The American Statistician*, vol. 43, no. 1, pp. 50–54, 1989.

[63] D. C. Hoaglin, B. Iglewicz, and J. W. Tukey, "Performance of some resistant rules for outlier labeling," *Journal of the American Statistical Association*, vol. 81, no. 396, pp. 991–999, 1986.

[64] N. C. Schwertman and R. de Silva, "Identifying outliers with sequential fences," *Computational Statistics & Data Analysis*, vol. 51, no. 8, pp. 3800–3810, 2007.

[65] S. Garg, K. Kaur, N. Kumar, G. Kaddoum, A. Y. Zomaya, and R. Ranjan, "A hybrid deep learning-based model for anomaly detection in cloud datacenter networks," *IEEE Transactions on Network and Service Management*, vol. 16, no. 3, pp. 924–935, 2019.